Probing gas kinematics towards the high-mass protostellar object G358.46–0.39

C Ugwu, J Chibueze, J Morgan, T Csengeri, A Chukwude, D van der Walt, J Alhassan

To cite this version:

C Ugwu, J Chibueze, J Morgan, T Csengeri, A Chukwude, et al.. Probing gas kinematics towards the high-mass protostellar object G358.46–0.39. Monthly Notices of the Royal Astronomical Society, 2023, 520 (3), pp.4747-4759. 10.1093/mnras/stad376. hal-04298976

HAL Id: hal-04298976
https://hal.science/hal-04298976v1

Submitted on 25 Jan 2024

Monthly Notices
of the
ROYAL ASTRONOMICAL SOCIETY

MNRAS **520,** 4747–4759 (2023) https://doi.org/10.1093/mnras/stad376
Advance Access publication 2023 February 2

Probing gas kinematics towards the high-mass protostellar object G358.46−0.39

C. J. Ugwu,[1,2]★ J. O. Chibueze ,[1,3]★ J. Morgan ,[3]★ T. Csengeri,[4] A. E. Chukwude,[1] D. J. van der Walt[3] and J. A. Alhassan[1]

[1] *Department of Physics and Astronomy, Faculty of Physical Sciences, University of Nigeria, Carver Building, 1 University Road, Nsukka, 410001, Nigeria*
[2] *Department of Science Laboratory Technology, Faculty of Physical Sciences, University of Nigeria, Carver Building, 1 University Road, Nsukka 410001, Nigeria*
[3] *Centre for Space Research, Potchefstroom Campus, North-West University, Potchefstroom 2520, South Africa*
[4] *Laboratoire d'astrophysique de Bordeaux, Univ. Bordeaux, CNRS, B18N, allée Geoffroy Saint-Hilaire, F-33615 Pessac, France*

Accepted 2023 January 30. Received 2023 January 28; in original form 2022 January 31

ABSTRACT

We investigated the nature of protostellar objects in G358.46−0.39 and their gas kinematics using ALMA data, with the aim of understanding the ongoing star formation activities in the region. The dust continuum map reveals multiple cores (MM1a, MM1b, MM1c, and MM2) dominated by MM1a, with no detectable free–free emission. We calculated the masses and the column densities of the various objects (MM1a, MM1b, MM1c, and MM2). A total of 33, 10, 10, and 9 molecular transitions are detected towards MM1a, MM1b, MM1c, and MM2, respectively. The differences in the number of molecular lines detected towards each of the cores support different excitation conditions at different positions. We derived the kinetic temperature ranges of MM1a, MM1b, MM1c, and MM2 to be ∼96–118, 96–114, 72–74, and 80–84 K, respectively. A highly collimated bipolar outflow traced by ^{12}CO emission is observed to be associated with MM1a, with knots along the outflow lobes, which could be an indication of episodic ejection. The C^{17}O emission is observed to be likely tracing a slowly rotating envelope of gas around MM1a. The velocity field map of CH$_3$OH ($2_{2,\,1} - 3_{1,\,2}$) emission suggests the presence of a rotating structure, possibly a disc. The physical and kinematic properties of MM1a are strong indication of a massive young stellar object, with ongoing outflow activity and accretion in its early stage of formation.

Key words: line: identification – methods: observational – techniques: interferometric – software: data analysis – stars: individual: G358.46−0.39 – submillimetre: stars.

1 INTRODUCTION

Despite numerous researches on high-mass star formation, the early formative stages of massive stars are still poorly understood. This is partly attributed to the fact that they are deeply embedded in molecular clouds, which are highly obscured by circumstellar dust with high extinction ($A_V \geq 10$) and are mostly located at far distances (≥1 kpc), making them very difficult to be observed at infrared and optical wavelengths (see review by Zinnecker & Yorke 2007). Nevertheless, observational studies of high-mass star formation continue to gain more attention and interests as a result of enhanced sensitivities and angular resolutions, offered by upgraded and newly developed instruments around the world.

Outflows and jets are prominent features of early stages of (high-mass) star formation and as such, their study provides some insight into the early evolutionary phase of massive stars (e.g. Cesaroni et al. 2007; Bachiller 2009; Ginsburg et al. 2018; Sanna et al. 2019; Zhao et al. 2020). These phenomena are thought to be responsible for the regulation of some star formation processes, such as the removal of excess angular momentum emanating from a disc-driven outflow system and the dispersion of the parent molecular cloud (Bachiller 1996; Cesaroni et al. 2007; Bachiller 2009). Outflows are strong tools for dating the accretion history of protostellar objects. The morphology and collimation of outflow changes with time, thus, can be used as a clock for core evolution. Outflows seen in youngest cores are strongly collimated whereas those associated with older cores show much lower collimation factors (Arce et al. 2007). This is because the youngest cores are believed to still be in their main accretion phase with highly collimated jets while the older cores are thought to be associated with strong wide-angle winds with no accompanying jets (Arce et al. 2007). In addition, outflows and discs give information about the kinematics of circumstellar gas in young stellar objects (YSOs). Molecular line emissions from massive young stellar objects (MYSOs) serve as outflows (e.g. CO), jets (e.g. SiO), and discs (e.g. CH$_3$CN) tracers, which are observed at submillimetre/millimetre wavelengths, unaffected by dust extinction. In this context, Atacama Large Millimeter/Submillimeter Array (ALMA) provides an excellent opportunity to investigate the kinematics of circumstellar gas in MYSOs, especially the outflows, jets, and discs in YSOs of all masses up to at least 20 M$_\odot$ (Ginsburg et al. 2018; Sanna et al. 2019).

G358.46−0.39 is a well-known high-mass protostellar object (Chibueze et al. 2017; Csengeri et al. 2017) associated with a periodic 6.7 GHz class II methanol maser source (Maswanganye et al. 2015). Based on the Galactic rotation curve of Reid et al.

★ E-mail: jude.ugwu@unn.edu.ng (CJU); james.chibueze@gmail.com (JOC); jeanmariemorgan0@gmail.com (JM)

Published by Oxford University Press on behalf of Royal Astronomical Society

(2009), Chen et al. (2013) estimated the kinematic distance to G358.46−0.39 to be ∼2.9 kpc. Molecular outflows associated with the object are reported in Chen et al. (2013). Caswell et al. (2010) reported that G358.46−0.39 is a pair of sources (G358.460−0.391 and G358.460−0.393) separated from each other by 7 arcsec and located at Galactocentric radius, $R > 3.5$ kpc. Chen et al. (2013) noted that extended green object (EGO) pair exists in G358.46−0.39, which are G358.46−0.39 (a) and G358.46−0.39 (b). The authors found that the physical and kinematic properties derived from 3 mm molecular lines for G358.46−0.39 are consistent with the source being MYSO with ongoing outflow activity and rapid accretion in its earliest evolutionary stage. According to Chen et al. (2013), the line wing emission from CS and HNC line associated with G358.46−0.39 is from both blueshifted and redshifted (double) wings, which is suggestive of bipolar outflow activity. From Gaussian fit to the N_2H^+ line, the systemic velocity of G358.46−0.39 is -3.36 ± 0.01 km s^{-1} (Chen et al. 2013). Csengeri et al. (2017) revealed from continuum emission observations that G358.46−0.39 consists of two emission cores, which are G358.46−0.39 MM1 (hereafter MM1) and G358.46−0.39 MM2 (hereafter MM2), with corresponding core mass of 218.09 and 81.92 M$_\odot$, respectively. The authors estimated a kinematic distance of 5 kpc to the source, which was adopted in their mass estimation. The distance estimates (2.9 and 5 kpc) to the source by Chen et al. (2013) and Csengeri et al. (2017) are both from kinematic distance estimation, and Csengeri et al. (2017) also considered the larger scale environment of the region. Kinematic distance produces two distance namely near and far distance, resulting in kinematic distance ambiguity. A more reliable distance measurement (i.e. parallax distance estimation) to the source is yet to be determined. In this work, we estimated a near kinematic distance of 3.9 kpc to the source, based on the revised kinematic distance estimation of Reid et al. (2014). The local standard of rest velocity (systemic velocity) used for the distance estimation is −3.1 km s^{-1}, obtained from Gaussian fit to the SO_2 ($19_{1,\,19} - 18_{0,\,18}$) line in this work. This recent near kinematic distance of 3.9 kpc to the source was adopted in this work. Both MM1 and MM2 are associated with 6.7 GHz class II methanol maser sources (Chibueze et al. 2017). According to Maswanganye et al. (2015), MM1 shows periodic flux variability in 6.7 GHz methanol maser emission, with a period of 220.0 ± 0.2 d, while MM2 reveal no significant flux variability in 6.7 GHz methanol maser emission. There are no existing information on the chemical richness of MM1 and MM2 and their respective gas kinematics. In order to better understand the nature and the molecular richness of cores in the source, it is important to identify the actual number of cores in the object and the molecular species associated with each core, using high angular resolution ALMA continuum and spectral line data of G358.46−0.39.

In this submission, we analysed the continuum and spectral line ALMA data of G358.46−0.39 using Common Astronomy Software Applications (CASA) package in order to investigate the protostellar nature and kinematics of the source, with the aim to pin down the physical conditions of the ongoing star formation. The work disentangled the multiplicity nature of the source, with several cores exhibiting different molecular spectra. The observations and results are, respectively, presented in Sections 2 and 3, while Sections 4 and 5 are the discussion and conclusions, respectively.

2 OBSERVATIONS

The archival ALMA data of G358.46−0.39 with project code 2013.1.00960.S, (PI: Csengeri T) was used in this work. The continuum and spectral line data of G358.46−0.39 were obtained from the ALMA Science Archive[1] to analyse G358.46−0.39, using CASA (4.3.1) package. The observations have been carried out on 2014 June 14 in ALMA band 7 during the cycle 2 with Atacama Compact Array (ACA), using 9–11 of the 7 m antennas. The shortest and longest baselines are 8.2 and 48.9 m, respectively, achieving an angular resolution of 9″.1 × 2″.6. Another observation was carried out on 2015 April 8 using ALMA 12 m array (36 antennas), with baselines ranging from 15.1 to 348.5 m, achieving an angular resolution of 0″.9 × 0″.6. J1924−2914, J1717−3342, and Titan were used as the bandpass, complex gain, and amplitude calibrators, respectively. The water vapour radiometres provided the water column information used for reducing the atmospheric phase noise.

The spectral configurations of the 7 and 12 m array observations are identical. The lowest spectral resolution mode of the four baseband channels used was centred on 347.331, 345.796, 337.061, and 335.900 GHz, respectively, resulting to 4 × 1.75 GHz effective bandwidth, with a spectral resolution of 976.562 kHz. The primary beam size at this frequency is 28″.9. The four baseband channels ranging from 333.419 to 335.292, 335.293 to 337.167, 345.334 to 347.208, and 347.167 to 349.041 GHz, correspond to spectral window (spw) 3, 2, 1, and 0, respectively.

The data were calibrated using standard procedures in CASA 4.3.1 program. The line-free continuum maps were obtained by excluding the channels with spectral lines above $3\sigma_{\rm rms}$ per channel and then averaged the remaining channels. For imaging, the CLEAN algorithm, with a Brigg robust weight of 0.5, favouring sensitivity, was used for the deconvolution. The synthesized beam size is 0″.97 × 0″.65, with a position angle of −89.2°. The geometric mean of the major and minor axes corresponds to a beam size of 0″.81 (∼3200 au at the adopted distance for the source). The achieved rms noise level in the continuum is 3 mJy beam^{-1}.

The cubes of the molecular line emission were created by subtracting the continuum determined in emission free channels around the selected line and corrected for primary beam attenuation. For the analysis, we used only the 12 m data, since our main interest is on the molecular emission that originates from scales typically smaller than the largest angular scales of ∼7 arcsec, beyond which the sensitivity of the 12 m array observations declines. As such, no information from the more compact 7 m array observations was used for the analysis. More details on the observations and data reduction are found in Csengeri et al. (2017, 2018, 2019).

3 RESULTS

3.1 G358.46−0.39 continuum emission

The ALMA 0.9 mm observations reveal a number of dust continuum cores dominated by MM1a (see Fig. 1), which hosts the periodic 6.7 GHz methanol maser (indicated with a white cross in Fig. 1) in the region. There are two other unresolved dust continuum objects, MM1b and MM1c, located ∼2.3 and ∼3.7 arcsec south-east of MM1a. MM2 is located ∼7.3 arcsec south-east of MM1a and associated with a non-periodic methanol maser. From the recent 1.28 GHz Galactic Plane Survey carried out with the MeerKAT telescope (Goedhart et al., in preparation), we found an unresolved ultracompact H II region indicated as cyan contours in Fig. 1. There are three other dust emission cores marginally detected (∼3σ) south of MM1b, south-east of MM2 and south of MM2. These sources

---

[1] http://almascience.eso.org/aq/

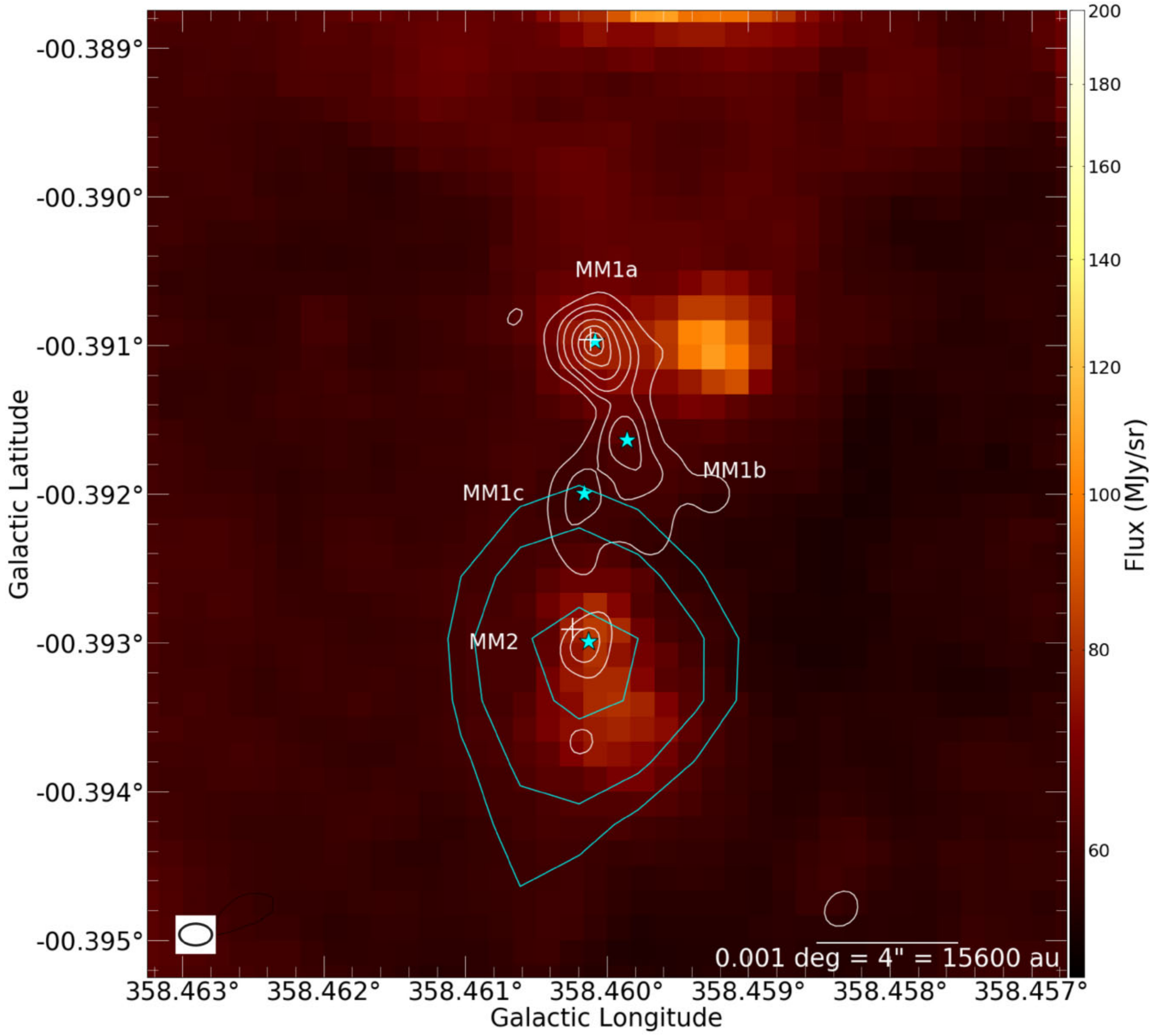

Figure 1. Composite image of G358.46−0.39. Background is 8 μm Spitzer infrared image while the white contours (levels = 15, 30, 45, 75, 105, 135 mJy beam^{-1}) represent the 0.9 mm ALMA dust continuum emission. The cyan contours (levels = 10, 30, 60 μJy beam^{-1}) represent the MeerKAT 1.28 GHz image of a faint free–free emission peaked around MM2 object. The position of the 6.7 GHz methanol maser sources are indicated by the white crosses while the cyan stars indicate the peak positions of the ALMA continuum cores. The beam sizes of ALMA (represented by the black ellipse on the botton left corner) and MeerKAT are $0\farcs97 \times 0\farcs65$ and $7\farcs99 \times 7\farcs99$, respectively.

Table 1. Summary of results of the continuum parameters.

Object name	RA (J2000) (h m s)	Dec. (J2000) (° ′ ″)	Peak intensity (mJy beam^{-1})	Integrated flux (mJy)	Size (arcsec × arcsec [P.A.]°)	T_d (K)	Core mass (M$_\odot$)	N_{H_2} (10^{25} cm^{-2})
G358.46−0.39 MM1a	17 43 26.7	−30 27 11.7	137 ± 6	298 ± 19	1.2 × 0.5 [164]	100 − 200	344 − 172	5.3 − 2.6
G358.46−0.39 MM1b	17 43 26.8	−30 27 13.5	48.3 ± 1.4	134 ± 5	1.4 × 0.7 [136]	100 − 200	155 − 77	1.6 − 0.8
G358.46−0.39 MM1c	17 43 27.0	−30 27 13.2	30.9 ± 1.2	96.3 ± 8.3	1.8 × 1.1 [109]	100 − 200	111 − 56	0.6 − 0.3
G358.46−0.39 MM2	17 43 27.2	−30 27 15.2	41.2 ± 0.8	74 ± 2	1.1 × 0.8 [106]	100 − 200	85 − 43	1.0 − 0.5

are not considered in this paper. Two-dimensional Gaussian fit in the image plane was used to extract the properties (such as the position, peak intensity, integrated flux, and core size) of the bulk emission of the various dust continuum cores. Details of each detected cores derived from two-dimensional Gaussian fit of the continuum around each core are presented in Table 1.

The unresolved MeerKAT 1.28 GHz radio continuum emission associated with MM2 is an indication of the existence of H II

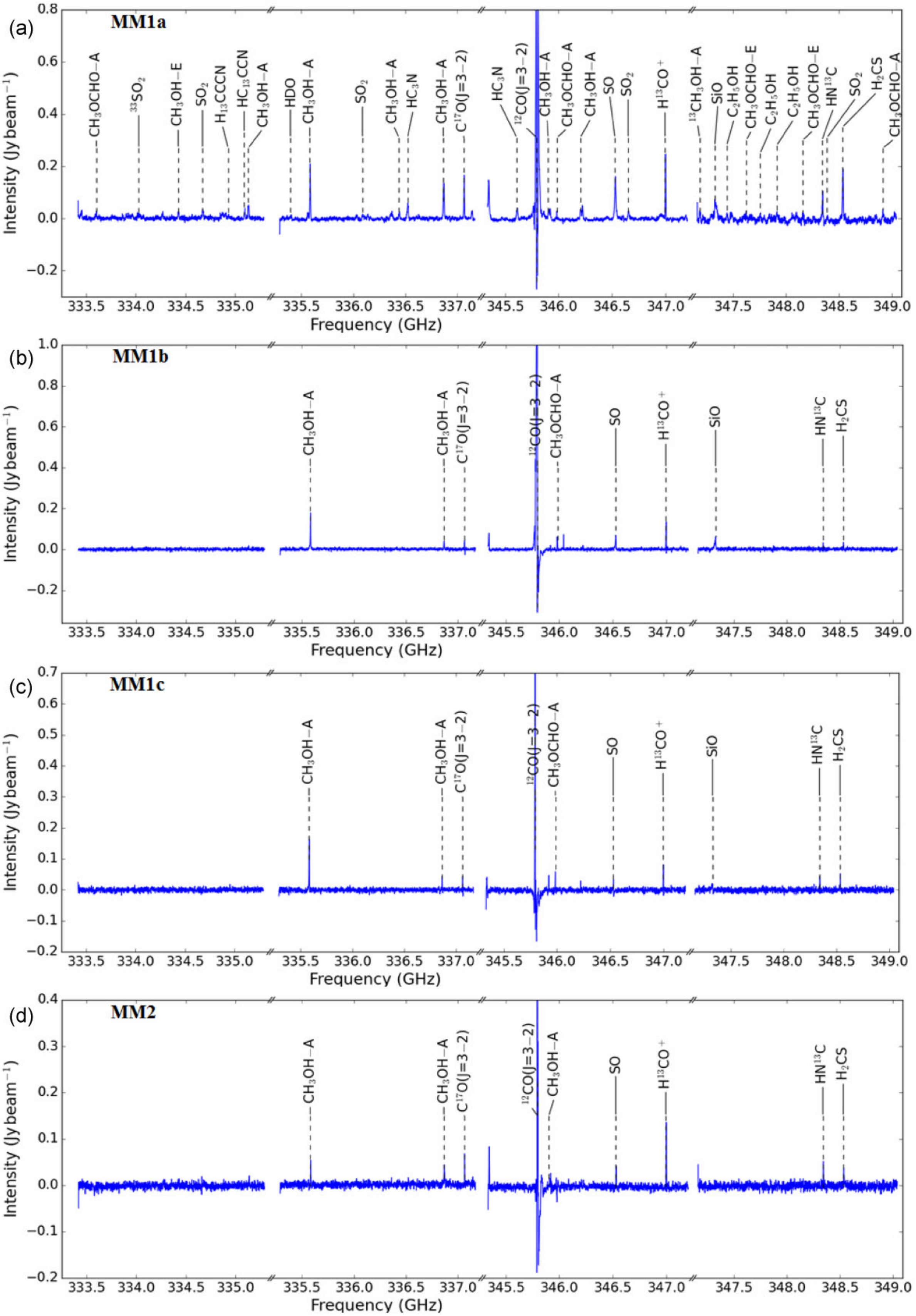

Figure 2. ALMA band 7 spectra for each dust continuum object.

Table 2. Features of the identified spectral lines towards 0.9 mm continuum peak of MM1a, for the four spectral windows.

Molecular species	Transitions	Frequency (GHz)	$\mathrm{Log}_{10}(A_{ij})^a$ (s^{-1})	E_{up}/k^b (K)	Data base	Observed intensity (Jy beam^{-1})	Linewidth (kms^{-1})
$CH_3OCHO{-}A$ ($v_t = 0$)	$27_{4,\,23} - 26_{4,\,22}$	333.601	−3.265	241	JPL	0.028 ± 0.003	3.5 ± 0.2
$CH_3OCHO{-}A$ ($v_t = 0$)	$28_{12,\,17} - 27_{12,\,16}$	345.985	−3.287	335	JPL	0.031 ± 0.004	3.5 ± 0.3
$CH_3OCHO{-}E$ ($v_t = 0$)	$28_{10,\,19} - 27_{10,\,18}$	347.628	−3.260	307	JPL	0.028 ± 0.004	5.2 ± 0.2
$CH_3OCHO{-}E$ ($v_t = 1$)	$25_{13,\,13} - 25_{12,\,14}$	348.159	−4.330	491	JPL	0.023 ± 0.005	5.9 ± 0.3
$CH_3OCHO{-}A$ ($v_t = 0$)	$28_{9,\,20} - 27_{9,\,19}$	348.915	−3.235	295	CDMS	0.035 ± 0.005	7.1 ± 0.2
$^{33}SO_2$	$23_{3,\,21} - 23_{2,\,22}$	334.030	−3.586	279	CDMS	0.022 ± 0.005	12.9 ± 0.1
SO_2	$8_{2,\,6} - 7_{1,\,7}$	334.673	−3.896	43	CDMS	0.035 ± 0.001	5.5 ± 0.3
SO_2	$23_{3,\,21} - 23_{2,\,22}$	336.089	−3.573	276	CDMS	0.017 ± 0.007	5.4 ± 0.5
SO_2	$19_{1,\,19} - 18_{0,\,18}$	346.652	−3.282	168	CDMS	0.031 ± 0.005	11.2 ± 0.4
SO_2	$24_{2,\,22} - 23_{3,\,21}$	348.387	−3.719	293	CDMS	0.015 ± 0.005	3.5 ± 0.3
$CH_3OH{-}E$ ($v_t = 1$)	$3_{-0,\,3} - 2_{-1,\,2}$	334.426	−4.255	315	CDMS	0.025 ± 0.002	15.2 ± 0.1
$CH_3OH{-}A$ ($v_t = 0$)	$2_{2,\,1} - 3_{1,\,2}$	335.134	−4.569	45	CDMS	0.059 ± 0.003	10.7 ± 0.4
$CH_3OH{-}A$ ($v_t = 0$)	$7_{1,\,7} - 6_{1,\,6}$	335.582	−3.788	79	CDMS	0.209 ± 0.005	7.2 ± 0.1
$CH_3OH{-}A$ ($v_t = 0$)	$14_{7,\,7} - 15_{6,\,9}$	336.438	−4.441	488	CDMS	0.026 ± 0.005	13.2 ± 0.3
$CH_3OH{-}A$ ($v_t = 0$)	$12_{1,\,11} - 12_{0,\,12}$	336.865	−3.390	197	CDMS	0.136 ± 0.003	8.6 ± 0.2
$CH_3OH{-}A$ ($v_t = 0$)	$16_{1,\,15} - 15_{2,\,14}$	345.903	−3.982	333	CDMS	0.039 ± 0.003	21.8 ± 0.2
$CH_3OH{-}A$ ($v_t = 0$)	$5_{4,\,1} - 6_{3,\,4}$	346.204	−4.662	115	CDMS	0.052 ± 0.003	1.9 ± 0.1
$^{13}CH_3OH{-}A$ ($v_t = 0$)	$14_{1,\,13} - 14_{0,\,14}$	347.188	−3.360	254	CDMS	0.029 ± 0.005	3.5 ± 0.2
$H^{13}CCCN$	J = 38 − 37	334.930	−2.523	314	JPL	0.018 ± 0.004	1.8 ± 0.2
$HC^{13}CCN$	J = 37 − 36	335.092	−2.521	306	CDMS	0.039 ± 0.004	5.2 ± 0.1
HDO	$3_{3,\,1} - 4_{2,\,2}$	335.395	−4.583	335	JPL	0.016 ± 0.002	9.1 ± 0.3
HC_3N	J = 37 − 36	336.520	−2.516	307	CDMS	0.149 ± 0.008	15.5 ± 0.6
HC_3N	J = 38 − 37	345.609	−2.481	324	CDMS	0.132 ± 0.007	13.3 ± 0.5
$C^{17}O$	J = 3 − 2	337.061	−5.879	32	CDMS	0.181 ± 0.005	5.3 ± 0.4
^{12}CO	J = 3 − 2	345.795	−5.602	33	CDMS	0.898 ± 0.004	22.8 ± 0.3
SO	$J = 9_8 - 8_7$	346.528	−3.269	79	CDMS	0.163 ± 0.003	6.9 ± 0.2
$H^{13}CO^+$	J = 4 − 3	346.998	−2.483	42	CDMS	0.249 ± 0.003	4.3 ± 0.1
SiO	J = 8 − 7	347.330	−2.656	75	CDMS	0.068 ± 0.002	14.1 ± 0.1
C_2H_5OH	$21_{1,\,21} - 20_{0,\,20}$	347.445	−3.349	186	CDMS	0.022 ± 0.006	7.1 ± 0.3
C_2H_5OH	$38_{2,\,36} - 38_{2,\,37}$	347.759	−4.976	682	CDMS	0.022 ± 0.005	7.1 ± 0.2
C_2H_5OH	$20_{4,\,17} - 19_{4,\,16}$	347.915	−3.421	251	CDMS	0.027 ± 0.003	6.9 ± 0.1
$HN^{13}C$	J = 4 − 3	348.340	−2.797	42	JPL	0.105 ± 0.003	3.2 ± 0.1
H_2CS	$10_{1,\,9} - 9_{1,\,8}$	348.534	−3.199	105	CDMS	0.189 ± 0.006	7.3 ± 0.4

Notes.

[a] Einstein coefficient (A_{ij}) in per second (s^{-1}).

[b] Upper state excited energy level (E_{up}/k) in Kelvin (K).

region MM2. With the rms of $<6\,\mu$Jy beam^{-1}, the radio continuum is detected with more than 10σ signal-to-noise ratio. This is a demonstration of MeerKAT's power to detect faint emissions from young massive protostars.

Fig. 1 (background) shows 8 μm Spitzer image of the region. Faint, compact 8 μm emission is detected towards MM1a and MM2. Besides 6.7 GHz methanol masers, MM1 and MM2 are associated with a number of other maser species such as 22 GHz H_2O maser (Walsh et al. 2011, 2014; Titmarsh et al. 2016), 95 GHz CH_3OH maser (Yang et al. 2017), and near-infrared (NIR) objects (Lucas et al. 2008).

The dust mass, M_{d}, of each core can be estimated from

$$M_{\mathrm{d}} = \frac{S_\nu D^2}{\kappa_\nu B_\nu(T_{\mathrm{d}})}, \tag{1}$$

assuming optically thin dust emission (Hildebrand 1983). S_ν is the continuum integrated flux at frequency, ν, $B_\nu(T_{\mathrm{d}})$ is the Planck function at dust temperature, T_{d}, κ_ν is the dust opacity per unit mass, $\kappa_\nu = 0.0185\,\mathrm{cm}^2\mathrm{g}^{-1}$ at 345 GHz (Ossenkopf & Henning 1994), and D the distance to the source. $D \sim 3.9$ kpc was adopted in estimating the mass of each core. Observations show that star-forming regions that harbour hot cores have high temperatures more than 100 K (e.g. Brogan et al. 2009; Cyganowski et al. 2011) and cores within the vicinity of H II regions could be associated with high temperatures of more than 100 K (e.g. Osorio, Lizano & D'Alessio 1999; Mookerjea et al. 2007). Thus, in the absence of a line-temperature measurement, we adopted a range of dust temperature of 100–200 K, since MM1a is confirmed as a hot core, MM1b and MM1c evolving into hot cores (see Sections 3.2 and 4.3), while MM2 located within the vicinity of H II region (see Fig. 1). Using a gas-to-dust mass ratio of 100, the mass of the cores (MM1a, MM1b, MM1c and MM2) were estimated (see Table 1 for the derived values of the core masses).

The column densities, N_{H_2} of each core can be calculated using (e.g. Csengeri et al. 2019)

$$N_{\mathrm{H}_2} = \frac{S_\nu R}{B_\nu(T_{\mathrm{d}})\Omega\kappa_\nu\mu_{\mathrm{H}_2}m_{\mathrm{H}}}\ \mathrm{cm}^{-2}, \tag{2}$$

where Ω is the solid angle of the beam calculated by $\Omega = 1.13 \times \Theta^2$, where Θ is the geometric mean of the beam major and minor axes, R is the ratio of gas-to-dust (100), μ_{H_2} is the mean molecular weight per hydrogen molecule and is equal to 2.8, and m_{H} is the mass of a hydrogen atom. The derived values of column densities for the different cores are listed in Table 1.

The ionizing flux, S_* of the ultracompact H II region can be computed using the radio continuum integrated flux (see Martín-Hernández, Vermeij & van der Hulst 2005)

Table 3. Features of the identified spectral lines towards 0.9 mm continuum peak of MM1b, MM1c, and MM2, for the four spectral windows.

Molecular species	Transitions	Frequency (GHz)	$\mathrm{Log}_{10}(A_{ij})^{a}$ (s^{-1})	E_{up}/k^{b} (K)	Data base	Observed intensity (Jy beam^{-1})	Linewidth (kms^{-1})
		MM1b					
CH_3OH-A ($v_t = 0$)	$7_{1,7} - 6_{1,6}$	335.582	−3.788	79	CDMS	0.179 ± 0.004	4.1 ± 0.1
CH_3OH-A ($v_t = 0$)	$12_{1,11} - 12_{0,12}$	336.865	−3.390	197	CDMS	0.041 ± 0.005	4.9 ± 0.4
$C^{17}O$	$J = 3 - 2$	337.061	−5.879	32	CDMS	0.044 ± 0.004	2.3 ± 0.2
^{12}CO	$J = 3 - 2$	345.795	−5.602	33	CDMS	1.613 ± 0.002	3.6 ± 0.1
$CH_3OCHO-A$ ($v_t = 0$)	$28_{12,17} - 27_{12,16}$	345.985	−3.287	335	JPL	0.061 ± 0.004	1.9 ± 0.1
SO	$J = 9_8 - 8_7$	346.528	−3.269	79	CDMS	0.072 ± 0.002	1.8 ± 0.1
$H^{13}CO^+$	$J = 4 - 3$	346.998	−2.483	42	CDMS	0.137 ± 0.004	2.3 ± 0.2
SiO	$J = 8 - 7$	347.330	−2.656	75	CDMS	0.062 ± 0.005	11.1 ± 0.3
$HN^{13}C$	$J = 4 - 3$	348.340	−2.797	42	JPL	0.034 ± 0.007	2.3 ± 0.5
H_2CS	$10_{1,9} - 9_{1,8}$	348.534	−3.199	105	CDMS	0.035 ± 0.005	3.4 ± 0.2
		MM1c					
CH_3OH-A ($v_t = 0$)	$7_{1,7} - 6_{1,6}$	335.582	−3.788	79	CDMS	0.163 ± 0.003	3.4 ± 0.2
CH_3OH-A ($v_t = 0$)	$12_{1,11} - 12_{0,12}$	336.865	−3.390	197	CDMS	0.043 ± 0.005	2.6 ± 0.4
$C^{17}O$	$J = 3 - 2$	337.061	−5.879	32	CDMS	0.044 ± 0.007	1.3 ± 0.2
^{12}CO	$J = 3 - 2$	345.795	−5.602	33	CDMS	0.737 ± 0.003	1.8 ± 0.1
$CH_3OCHO-A$ ($v_t = 0$)	$28_{12,17} - 27_{12,16}$	345.985	−3.287	335	JPL	0.059 ± 0.004	1.7 ± 0.3
SO	$J = 9_8 - 8_7$	346.528	−3.269	79	CDMS	0.036 ± 0.003	1.5 ± 0.1
$H^{13}CO^+$	$J = 4 - 3$	346.998	−2.483	42	CDMS	0.082 ± 0.005	2.2 ± 0.4
SiO	$J = 8 - 7$	347.330	−2.656	75	CDMS	0.021 ± 0.003	10.5 ± 0.1
$HN^{13}C$	$J = 4 - 3$	348.340	−2.797	42	JPL	0.044 ± 0.002	2.1 ± 0.1
H_2CS	$10_{1,9} - 9_{1,8}$	348.534	−3.199	105	CDMS	0.053 ± 0.006	2.7 ± 0.3
		MM2					
CH_3OH-A ($v_t = 0$)	$7_{1,7} - 6_{1,6}$	335.582	−3.788	79	CDMS	0.055 ± 0.005	5.1 ± 0.4
CH_3OH-A ($v_t = 0$)	$12_{1,11} - 12_{0,12}$	336.865	−3.390	197	CDMS	0.044 ± 0.003	6.9 ± 0.1
CH_3OH-A ($v_t = 0$)	$16_{1,15} - 15_{2,14}$	345.903	−3.982	333	CDMS	0.027 ± 0.006	2.9 ± 0.3
$C^{17}O$	$J = 3 - 2$	337.061	−5.879	32	CDMS	0.068 ± 0.003	2.1 ± 0.2
^{12}CO	$J = 3 - 2$	345.795	−5.602	33	CDMS	0.402 ± 0.002	3.5 ± 0.1
SO	$J = 9_8 - 8_7$	346.528	−3.269	79	CDMS	0.041 ± 0.008	1.8 ± 0.1
$H^{13}CO^+$	$J = 4 - 3$	346.998	−2.483	42	CDMS	0.136 ± 0.004	2.8 ± 0.2
$HN^{13}C$	$J = 4 - 3$	348.340	−2.797	42	JPL	0.052 ± 0.005	2.6 ± 0.2
H_2CS	$10_{1,9} - 9_{1,8}$	348.534	−3.199	105	CDMS	0.037 ± 0.006	6.5 ± 0.5

Notes.
[a] Einstein coefficient (A_{ij}) in per second (s^{-1}).
[b] Upper state excited energy level (E_{up}/k) in Kelvin (K).

$$S_* = \frac{7.603 \times 10^{46}\mathrm{s}^{-1}}{b(\nu,\ T_{\mathrm{e}})}\left(\frac{S_\nu}{\mathrm{Jy}}\right)\left(\frac{T_{\mathrm{e}}}{10^4\mathrm{K}}\right)^{-0.33}\left(\frac{D}{\mathrm{kpc}}\right)^2, \qquad (3)$$

$$b(\nu,\ T_{\mathrm{e}}) = 1 + 0.3195\log\left(\frac{T_{\mathrm{e}}}{10^4\mathrm{K}}\right) - 0.2130\log\left(\frac{\nu}{\mathrm{GHz}}\right), \qquad (4)$$

where T_{e} is the electron temperature in the ionized plasma. Using a radio integrated continuum flux of 613 μJy, obtained from two-dimensional Gaussian fit of the radio continuum and adopted electron temperature of 6343 K, estimated for ultracompact H II region (Khan et al. 2022), the ionizing flux was calculated to be 9.0×10^{44} s^{-1} (corresponding to $\log(S_*) = 44.9$ s^{-1}). This suggests that the free–free emission is probably ionized by a B1 zero-age main-sequence (ZAMS) star.

3.2 G358.46−0.39 molecular line emission

The spectra (Fig. 2) extracted from a diameter of 0.″86 around the continuum peak position of the various cores (MM1a, MM1b, MM1c, and MM2), for all four spectral windows are identified with the aid of Cologne Database for Molecular Spectroscopy[2] (CDMS; Müller et al. 2005) and in some cases (where some of the spectroscopic information, such as the Einstein coefficient is not available in the CDMS) using the Jet Propulsion Laboratory[3] (JPL; Pickett et al. 1998) spectral line data base. The central frequency obtained from Gaussian fitting of each line profile is used to search for the line with the same corresponding frequency in CDMS. With the rms noise level of 4.7 mJy beam^{-1}, the threshold for line detection is $\geq 3\sigma$ signal-to-noise ratio, since most of the lines are weak. The identified lines are premised on the criteria that they are commonly detected in young forming stars (e.g. Brogan et al. 2009; Cyganowski et al. 2011; Hunter et al. 2014; Cunningham et al. 2016; Csengeri et al. 2019; Van Der Walt et al. 2021). A total of 33 lines from 14 molecular species are detected towards MM1a (Table 2). These lines are similar to what is seen in hot molecular cores (HMCs; e.g. Brogan et al. 2009; Cyganowski et al. 2011; Hunter et al. 2014; Cunningham et al. 2016). The 14 molecular species consist of seven oxygen-bearing molecules, four nitrogen-bearing molecules, and three sulphur-bearing molecules. The large number of organic transitions detected towards MM1a, suggests that it is an HMC (Van Dishoeck & Blake 1998).

---

[2] https://cdms.astro.uni-koeln.de/cgi-bin/cdmssearch

[3] https://spec.jpl.nasa.gov/ftp/pub/catalog/catform.html

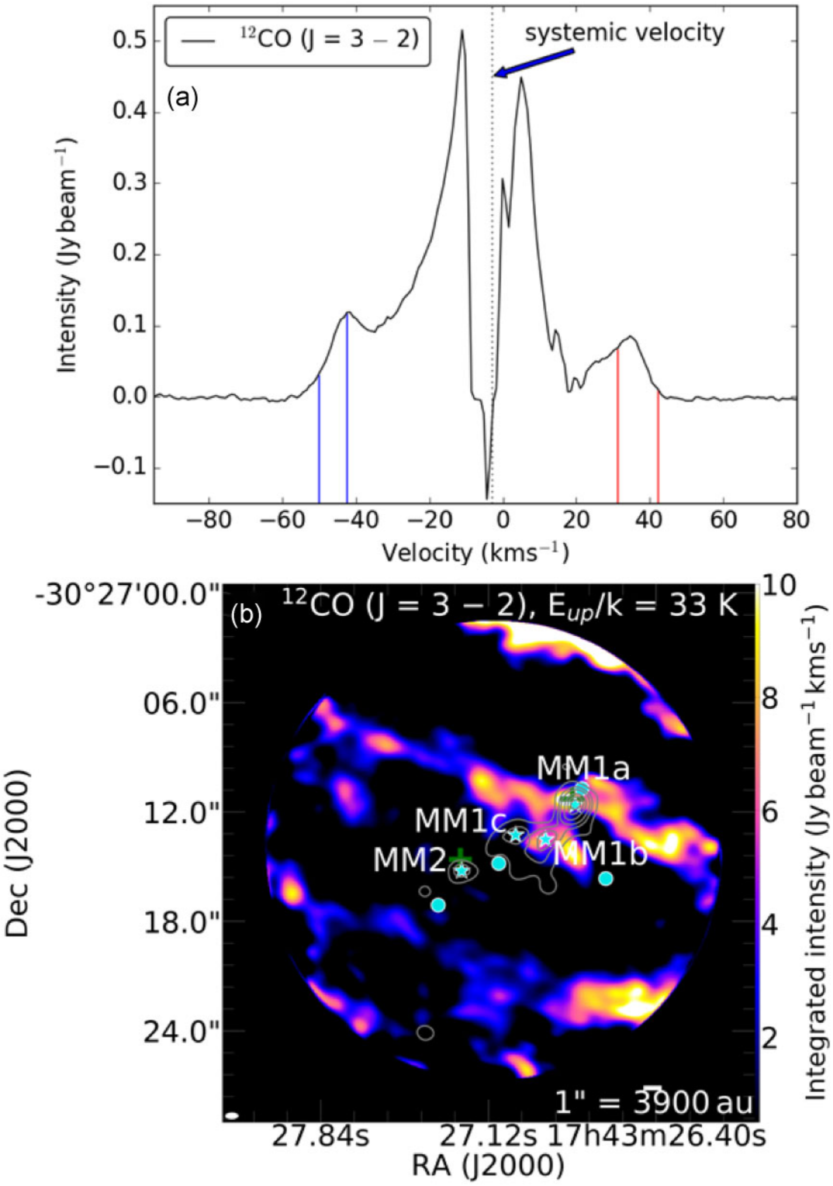

Figure 3. ^{12}CO line: (a) spectrum extracted from a diameter of 1″.07 around the continuum peak of MM1a and (b) zeroth moment map calculated between −44.1 and 38.9 kms^{-1}. The velocity range (−50.0 to −42.4 kms^{-1}) of the highly blueshifted wing is indicated by the blue lines. The velocity range (31.3–42.3 kms^{-1}) of the highly redshifted wing is marked by the red lines. The systemic velocity (−3.1 kms^{-1}) is indicated by the vertical dotted line. Grey contours (levels = 15, 30, 45, 75, 105, 135 mJy beam^{-1}) represent the 0.9 mm ALMA dust continuum emission. The position of the 6.7 GHz methanol maser sources are indicated by the green crosses. The cyan filled circles mark the position of the NIR objects obtained from UKIDSS Consortium (Lucas et al. 2008) within a radius of 5 arcsec from the 6.7 GHz methanol maser sources. Cyan stars are the same as in Fig. 1. The circular pattern with beam dilution shows the primary beam of ALMA. The synthesized beam is shown in the left bottom corner as a white ellipse.

The properties of the identified spectral lines for MM1b, MM1c, and MM2 are presented in Table 3. For MM1b, 10 lines from eight molecular species, consisting of five oxygen-bearing, one nitrogen-bearing, and two sulphur-bearing molecules are detected. A total of 10 transitions from eight molecular species, comprised of five oxygen-bearing, one nitrogen-bearing, and two sulphur-bearing molecules are detected towards MM1c. The detection of hot core tracers like CH_3OH and SO in MM1b and MM1c is an indication that these objects are evolving into hot cores. For MM2, nime transitions from six molecular species, consisting of three oxygen-bearing, one nitrogen-bearing, and two sulphur-bearing molecules are detected. The differences in the number of detected molecular emissions towards each of the cores (MM1a, MM1b, MM1c, and MM2) could be attributed to different evolutionary stages of the cores and excitation conditions at different positions (see SubSection 4.3).

3.2.1 CO molecular emissions

The ^{12}CO line spectrum (Fig. 3 (a)) extracted from a diameter of 1″.07 around the continuum peak of MM1a shows multiple peaks

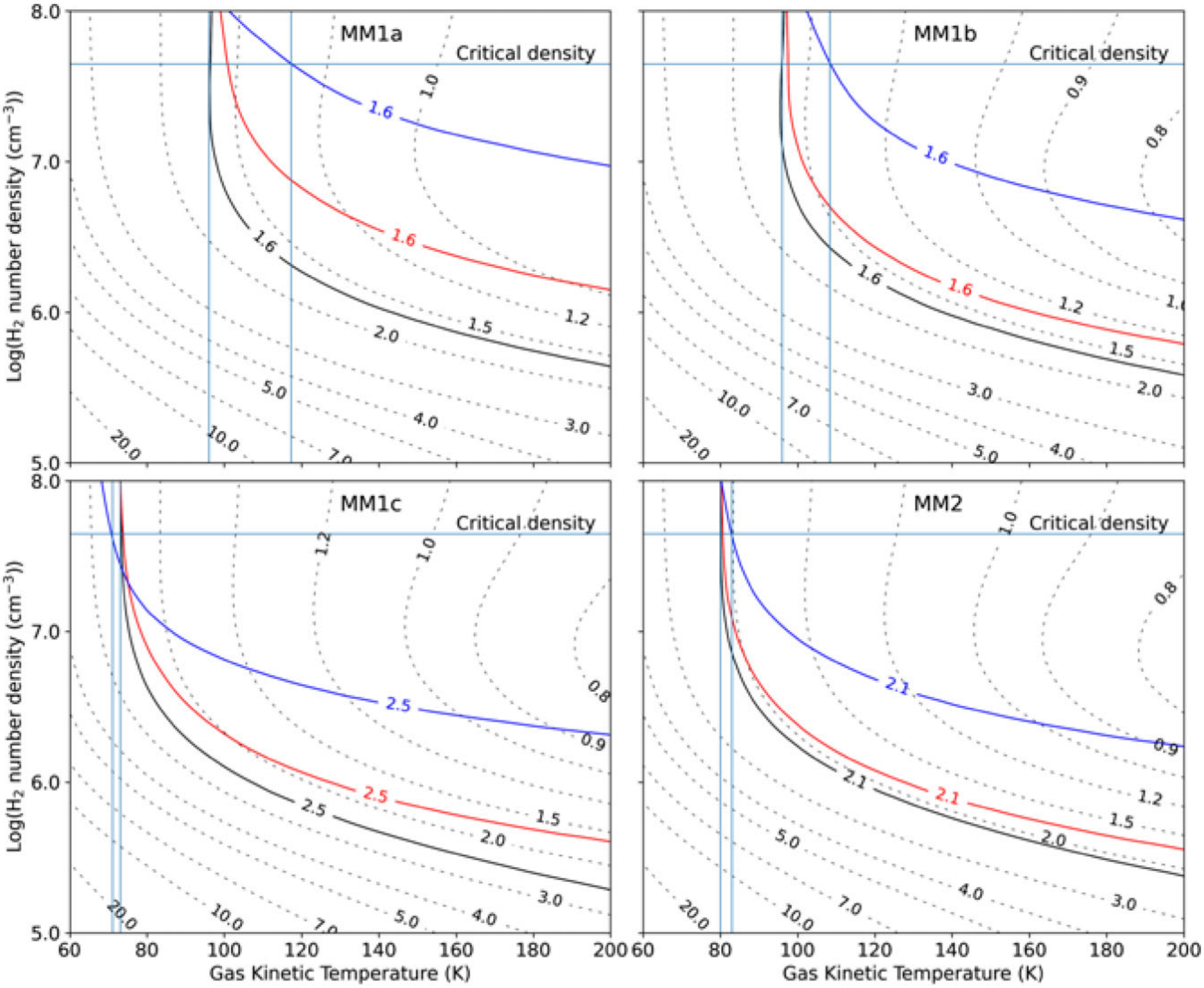

Figure 4. Variation of the ratio of the $7_{1,\,7}-6_{1,\,6}/12_{1,\,11}-12_{0,\,12}$ CH$_3$OH lines in the nH$_2-T_k$ plane for the various cores. The solid black line contour indicates the observed line ratio for a CH$_3$OH column density of 5.0×10^{14} cm^{-2} and line width of 7.9, 4.5, 3, and 6 kms^{-1} for MM1a, MM1b, MM1c, and MM2, respectively. The red line contour is for a column density of 5.0×10^{15} cm^{-2}. The blue line contour is for a column density of 5.0×10^{16} cm^{-2}. The dashed line contours represent an incorrect line ratio for a wrong CH$_3$OH column density and line width values.

and absorption features (the dips in the CO profile). The different CO peaks and absorption in the profile could be attributed to different cloudlets on the line of sight and CO self-absorption. The CO spectrum shows highly blueshifted and redshifted wings, which are unique features for bipolar emission. The velocity range of the highly blueshifted wing is from −50.0 to −42.4 kms^{-1} (blue lines) and that of the highly redshifted wing is from 31.3 to 42.3 kms^{-1} (red lines). The CO molecular emission is optically thick at the systemic velocity of the source (see the vertical dotted line within the dip in Fig. 3 (a)), while the CO emission associated with the wings is optically thin and reveals the CO bipolar emission. The integrated intensity (zeroth moment) map of the CO line calculated between −44.1 and 38.9 kms^{-1} is shown in Fig. 3 (b). The spatial distribution of CO molecules reveals complex morphology, with an elongated feature in the east–west of MM1a continuum peak position. This elongated feature in the east–west direction is an indication of bipolar outflow in MM1a. The CO emission is strongly affected by self-absorption (i.e. the dip in CO profile) and artefacts from poorly imaged large-scale emission (see also, Liu et al. 2017).

3.3 Estimate of gas kinetic temperature of the different cores

Further analysis in estimating the gas kinetic temperature for the various cores was carried out using the ratio of the $7_{1,\,7}-6_{1,\,6}/12_{1,\,11}-12_{0,\,12}$ CH$_3$OH lines as a function of H$_2$ number density (nH$_2$) and gas kinetic temperature (T_k), with the aid of RADEX (Van der Tak et al. 2007). Inspection of Table 2 shows that for MM1a, it is only these two CH$_3$OH lines that have similar line widths and that these are also the only CH$_3$OH lines detected in MM1b and MM1c. The collision coefficients used for the RADEX calculations are taken from the Leiden Atomic and Molecular Database[4] (LAMDA; Rabli & Flower 2010).

Fig. 4 shows the variation of the flux ratio of the $7_{1,\,7}-6_{1,\,6}$ and $12_{1,\,11}-12_{0,\,12}$ CH$_3$OH lines in the nH$_2-T_k$ plane, for the four cores. Calculation of the line ratios was done for CH$_3$OH column densities of 10^{14}, 10^{15}, and 10^{16} cm^{-2} and with a line width equal to the average of the widths of the two lines. In each panel, the dashed

---

[4] https://home.strw.leidenuniv.nl/moldata/CH3OH.html

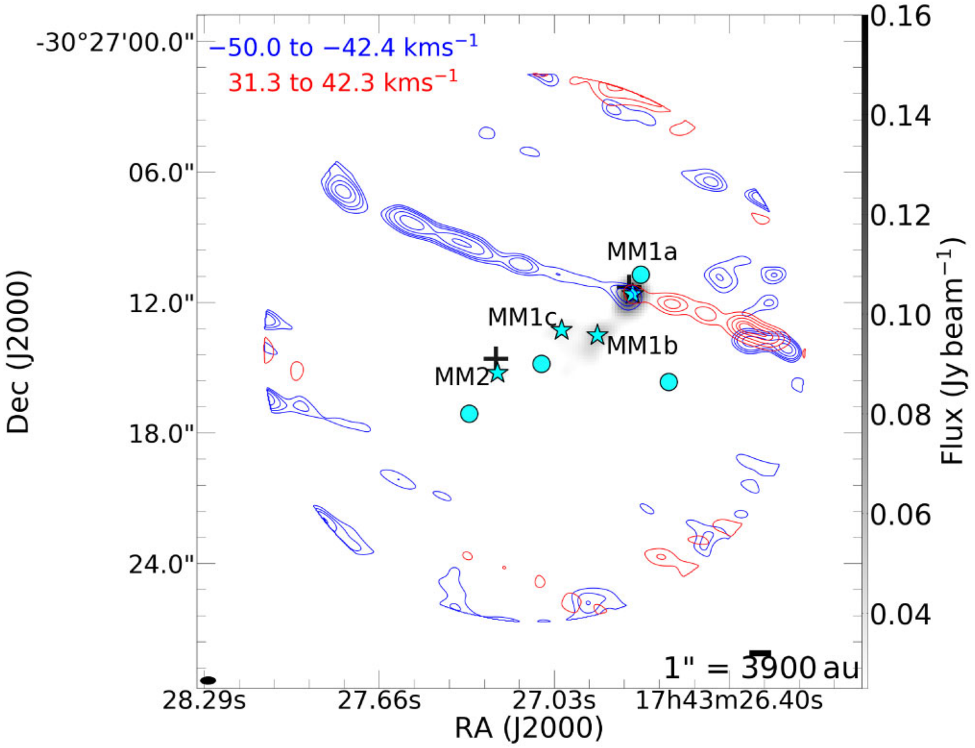

Figure 5. Collimated bipolar outflow of MM1a traced by ^{12}CO emission. The blue and red contours that indicate the blueshifted (−50.0 to −42.4 kms^{-1}) and redshifted (31.3 to 42.3 kms^{-1}) emission, respectively, are superimposed on a grey scale image of the dust continuum. The position of the 6.7 GHz methanol maser sources are indicated by the black crosses. Cyan filled circles and cyan stars are the same as in Fig. 3. The circular pattern with beam dilution shows the primary beam of ALMA. The synthesized beam is shown in the left bottom corner as a black ellipse.

contours show, for comparison, the variation of the flux ratio for a CH$_3$OH column density of 10^{14} cm^{-2}. The solid black, red, and blue lines are, respectively, the contours for the observed flux ratio for CH$_3$OH column densities of 10^{14}, 10^{15}, and 10^{16} cm^{-2}, with the observed flux ratio indicated in-line on the solid line contours for the four cores. To constrain the kinetic temperature range for each core, the critical density for the $12_{1,\,11} - 12_{0,\,12}$ line was calculated and found to be 4.4×10^{7} cm^{-3}. Using this value the kinetic temperature ranges of MM1a, MM1b, MM1c and MM2 are found to be ∼96–118, 96–114, 72–74, and 80–84 K, respectively, assuming that the levels population are dominated by collisions based on the derived $N_{\rm H_2}$ values in Table 1. The derived temperatures may have been affected by subthermal level population, especially in the less dense cores, which will imply that some of the line excitation may have occurred at densities lower than the critical density. It is important to note that the choice of constraining the kinetic temperature using the critical density is because we do not have line ratios of another molecule for which we can do the same analysis as for CH$_3$OH, in which the density and temperature are given by the point where the lines for CH$_3$OH and the other molecule intercept.

4 DISCUSSION

4.1 Highly collimated bipolar outflow

Jets, outflows, and collimated bipolar outflows are common among protostars at their early stages (Bally & Lada 1983; Gibb et al. 2003; Chibueze et al. 2012; Kölligan & Kuiper 2018). The ^{12}CO emission of MM1a exhibits evidence of collimated bipolar outflow. The ^{12}CO emission within the velocity ranges of the highly blueshifted and redshifted wings were extracted and imaged as blueshifted and redshifted emission. The integrated intensities blueshifted and redshifted contours are superimposed on the 0.9 mm continuum emission map shown in Fig. 5. The velocity range of the blueshifted integrated intensity contours is from −50.0 to −42.4 kms^{-1}, while the velocity range of the redshifted integrated intensity contours is from 31.3 to 42.3 kms^{-1}. The blueshifted lobe of the highly collimated bipolar outflow is located east of MM1a, while the redshifted lobe of the highly collimated bipolar outflow is distributed west of MM1a.

Both the blueshifted and redshifted lobes of the collimated outflow are associated with knots along the outflow lobes which could be an indication of episodic ejections (Torrelles et al. 2011; Burns et al. 2016). The blueshifted lobe extends 15″.2 (corresponding to ∼0.29 pc in projection at the adopted distance of 3.9 kpc) from the continuum peak position of MM1a to the eastern edge of the primary beam, while the redshifted lobe extends 8″.0 (corresponding to ∼0.15 pc in projection at the adopted distance of 3.9 kpc) from the continuum peak position of MM1a to the western edge of the primary beam.

4.2 Rotating envelope structure and a possible disc

Rotation structures (discs or envelopes) are becoming quite common among massive protostellar objects (Johnston et al. 2015, 2020; Ilee et al. 2016). Typically, spatially compact and warmer molecular gas located close to the driving source with steeper velocity gradient trace the disc, while the spatially more extended molecular lines with less steep velocity gradient trace the envelope (Johnston et al. 2015; Bøgelund et al. 2019). MM1a is associated with a number of potential disc tracers like C^{17}O (J = 3 − 2) and CH$_3$OH ($2_{2,\,1} - 3_{1,\,2}$).

Fig. 6 (a) shows the integrated intensity (moment 0) map of C^{17}O (with an angular size of ∼2″.9, corresponding to ∼11 310 au). The spatial distribution of C^{17}O (Fig. 6 (a)) molecules reveals an extended

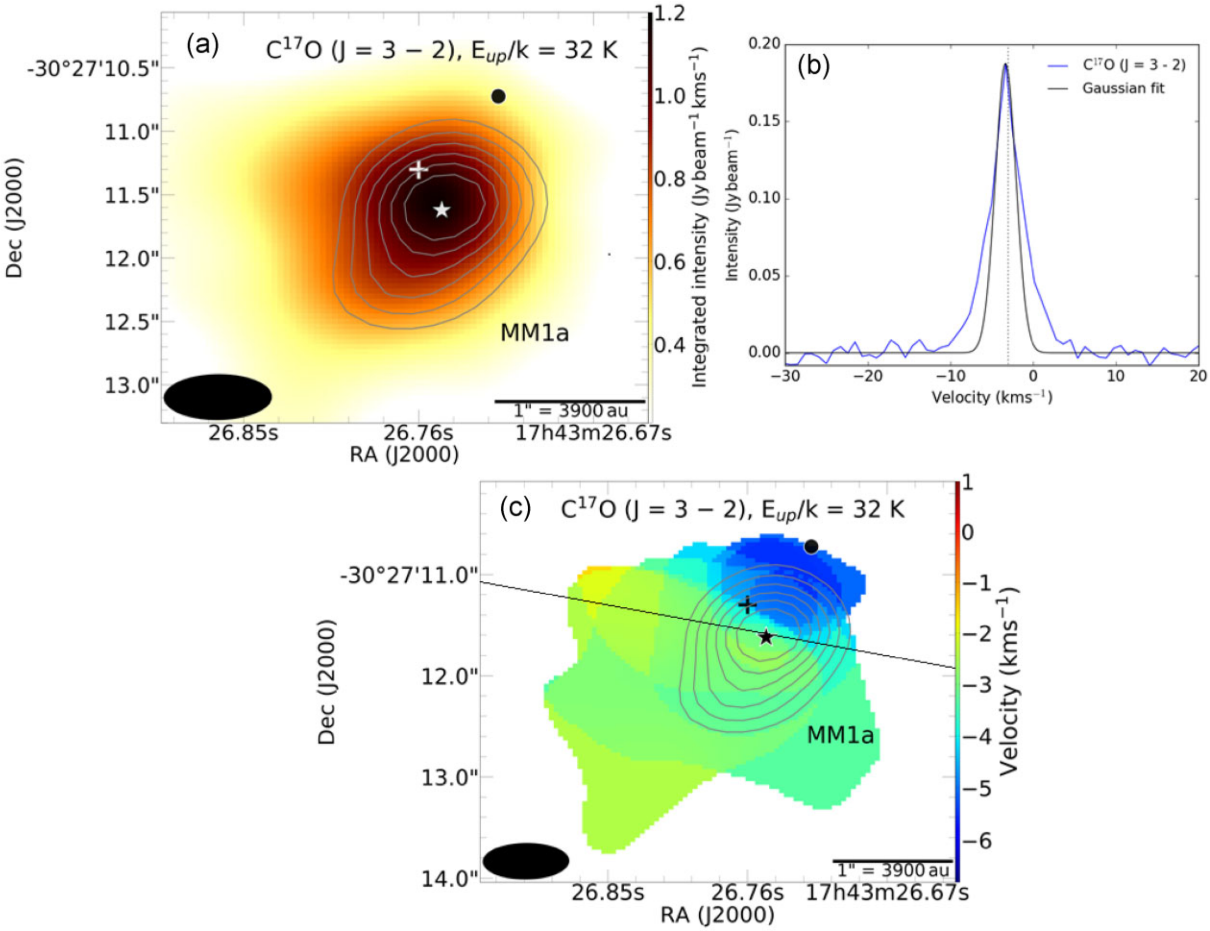

Figure 6. C^{17}O (J = 3 − 2) line: (a) integrated intensity (zeroth moment) map calculated between −6.8 and 1.0 kms^{-1}, (b) spectrum extracted from a diameter of 0.″86 around the continuum peak position of MM1a, and (c) velocity field (first moment) map from −6.8 to 1.0 kms^{-1}. The grey contours (levels = 60, 75, 90, 105, 120, 135 mJy beam^{-1}) represent the 0.9 mm ALMA dust continuum emission. The black line represents the direction of the bipolar outflow traced by CO emission (see Section 4.1). The position of the 6.7 GHz methanol maser source is indicated by the white and black crosses. The black filled circle marks the position of the NIR objects obtained from UKIDSS Consortium (Lucas et al. 2008) within a radius of 5 arcsec from the 6.7 GHz methanol maser source. The position of the continuum peak of MM1a is indicated by the white and black stars. The black ellipse is the same as in Fig. 5. The vertical dotted line is the same as in Fig. 3 (a).

emission and its emission peaks at the position of MM1a. The extended emission of C^{17}O is likely tracing the outer envelope of the gas reservoir from which MM1a is formed. The C^{17}O spectrum (Fig. 6 (b)) also reveals narrow emission with unblended lines and its emission peaks at the systemic velocity of MM1a. This narrow profile, along with the spatially extended emission point to the possibility of C^{17}O tracing an outer envelope of gas around MM1a. The first moment map of C^{17}O (Fig. 6 (c)) shows a velocity gradient that resembles that of a slowly rotating envelope, with the most dominantly blueshifted emission extending north-west of the continuum peak position (black star), and the faint redshifted emission extending south-east of the continuum peak position.

Fig. 7 (a) shows the integrated intensity (moment 0) maps of CH$_3$OH (with an angular size of ∼1.″03, corresponding to ∼4020 au). The spatial distribution of CH$_3$OH (Fig. 7 (a)) molecule shows a compact morphology, with its emission peaking at the position of MM1a. We argue that the CH$_3$OH in the case of MM1a is tracing a rotating structure, possibly a disc. This suggestion is supported by its association with 6.7 GHz CH$_3$OH maser (known to mostly reside in the disc; Sugiyama et al. 2012). This maser is located ∼0.″5 (corresponding to ∼0.01 pc) from the centre of the CH$_3$OH emission and outside the peak emission of CH$_3$OH (see Fig. 7 (a) and (c)). The maser position was taken from the Australian Telescope Compact Array (ATCA; Caswell et al. 2010) with an astrometric accuracy of 0.″4. It is noteworthy that the CH$_3$OH line profile (Fig. 7 (b)) exhibits a clear pattern of high optical depth (with a plateau in the intensity profile) and peaks at the systemic velocity of MM1a.

Fig. 7 (c) shows the first moment map revealing the kinematics of the CH$_3$OH gas. The first moment map of CH$_3$OH ($2_{2,1} - 3_{1,2}$) emission (Fig. 7 (c)) reveals a clear velocity gradient, which is a signature of rotating structure (Johnston et al. 2015; Bøgelund et al. 2019). The redshifted emission extends south-east of the continuum peak position (black star), and the blueshifted emission extends north-west of the continuum peak position. The velocity pattern is consistent with rotational motions, with a clear velocity gradient almost perpendicular to the direction of the strong bipolar outflow seen in CO emission (see Section 4.1).

4.3 Molecular diversity of the different cores

Molecular diversity is observed in some massive protostellar objects, revealing several cores and the interpretation supports different

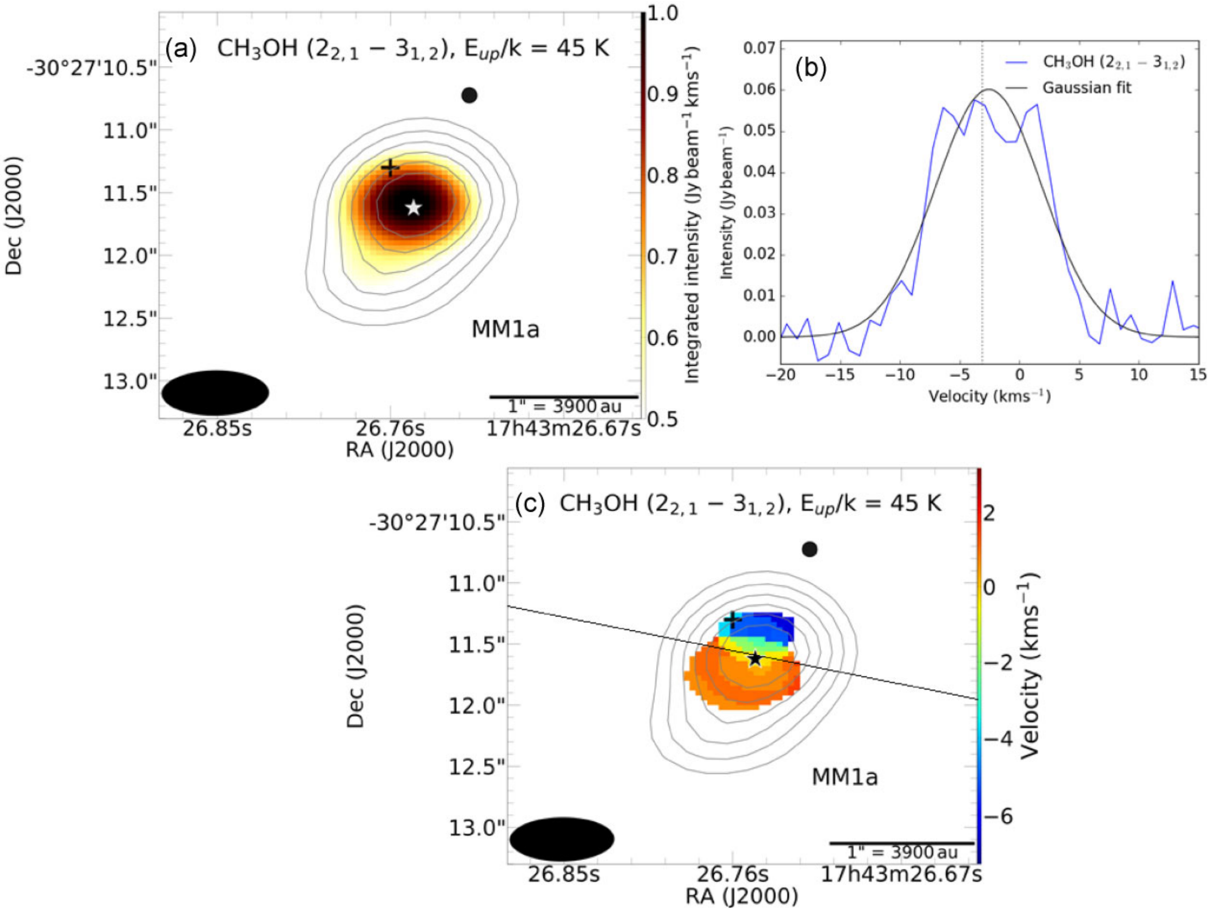

Figure 7. CH$_3$OH ($2_{2,\,1}-3_{1,\,2}$) line: (a) integrated intensity (zeroth moment) map calculated between −7.2 and 3.2 km s^{-1}, (b) spectrum extracted from a diameter of 0″.86 around the continuum peak position of MM1a, and (c) velocity field (first moment) map from −7.2 to 3.2 km s^{-1}. Black filled circle, black cross, white and black stars, black line, grey contours, black ellipse, and vertical dotted line are the same as in Fig. 6.

evolutionary stages of the cores (Brogan et al. 2009; Cyganowski et al. 2012) and/or varying molecular abundances in the various cores. MM1a, MM1b, MM1c, and MM2 showed different millimetre molecular spectra. MM1a exhibits forest of molecular lines (see Fig. 2 (a)). According to Herbst & van Dishoeck (2009), line forest detection is an indication of molecular complexity, which is usually associated with hot molecular cores. It follows therefore that MM1a has evolved into an HMC, since it is characterized by many lines. Complex oxygen-rich organic molecules (COMs; e.g. multiple transitions of CH$_3$OH and CH$_3$OCHO), which are characteristics of hot cores are seen towards MM1a (Herbst & van Dishoeck 2009; Rong et al. 2016; Liu et al. 2017). MM1a is the most chemically rich core, compared to MM1b, MM1c, and MM2 cores with few molecular line emission. The differences in chemical richness of the cores could be attributed to different evolutionary states of the cores.

MM1b and MM1c are both associated with star formation shock, high density, and outflow tracers like CH$_3$OH, SO, H^{13}CO$^+$, and CO transitions (see Fig. 2 (b) and (c)), confirming them as protostellar objects, but they are less chemically evolved than MM1a. This implies that MM1b and MM1c are insufficiently hot to excite COMs through desorption on to dust grain, resulting to lack of COMs in these poorly evolved cores (e.g. Di Francesco et al. 2007). MM2 also exhibits fewer molecular lines (see Fig. 2 (d)) than MM1a. However, MM2 is known to harbour H II region detected in the 1.28 GHz MeerKAT observations (Fig. 1). The lack of free–free emission in MM1a despite its chemical richness could indicate that MM1a is in an early evolutionary stage compared to MM2. The impact of the H II region in MM2 could have led to the dissociation of the COMs in MM2.

Other possibilities, such as observational biases (e.g. sensitivity issues, dust absorption, diluted emission, presence of substructures, etc.), different excitation conditions, intrinsic chemical diversity due to different dust grain mantle composition, might be responsible for the different observed millimetre spectra from the various cores (e.g. Brogan et al. 2009; Cyganowski et al. 2011, 2012; Hunter et al. 2014). For instance, the column densities of all molecular species are likely to be higher towards MM1a (with the highest column density, compared to MM1b, MM1c, and MM2, see Table 1) than towards the other cores (MM1b, MM1c and MM2), with lesser column densities, compared to MM1a. The lower intensities observed towards these other cores could, in principle, be due to differences in the total column densities and could also be attributed to different excitation conditions at different positions.

The derived temperatures (see Section 3.3) also give insights on the observed chemical diversity of the different cores. MM1a, with the highest gas kinetic temperature (average of 107 K) is associated with many molecular transitions compared to the other cores, supporting our argument that different excitation conditions might be responsible for the observed diversity in the molecular spectra of the different cores. On the other hand, sensitivity issues could be ruled out as one of the possibilities since the observations were very sensitive in detecting all the lines (including the weak lines) in all the positions. Therefore, the different observed millimetre spectra in all the positions are not due to limited sensitivity, but most likely favour the different excitation conditions at different positions.

5 CONCLUSIONS

We have presented a better understanding of the protostellar nature of G358.46−0.39 and its gas kinematics, using continuum and spectral lines Archival ALMA data of G358.46−0.39. Our analysis reveals multiple dust continuum cores (MM1a, MM1b, MM1c, and MM2) dominated by MM1a. MM1a harbours a periodic methanol maser while MM2 hosts a non-periodic methanol maser and associated with faint free–free emission. A total of 33 molecular lines from 14 molecular species, 10 lines from 8 molecular species, 10 lines from 8 molecular species, and 9 lines from 6 molecular species are identified towards MM1a, MM1b, MM1c, and MM2, respectively. This result supports different excitation conditions at different positions (MM1a, MM1b, MM1c, and MM2). MM1a is found to be the most chemically rich core and MM2 likely the most evolved core.

A highly collimated bipolar outflow traced by CO emission is seen towards MM1a, with knots along the outflow lobes, which could be an indication of episodic ejection. The C^{17}O emission is found to be likely tracing a slowly rotating envelope of gas from which MM1a is formed. The velocity pattern of CH$_3$OH ($2_{2,1} - 3_{1,2}$) emission is consistent with a velocity gradient almost perpendicular to the direction of the bipolar outflow, suggesting the presence of a rotating structure. The physical conditions of MM1a are strong indication of an MYSO with ongoing outflow activity and accretion in its early stage of formation. This work has provided, for the first time, information on the chemical richness of G358.46−0.39 cores.

ACKNOWLEDGEMENTS

This paper makes use of the following ALMA data: ADS/JAO.ALMA#2013.1.00960.S. ALMA is a partnership of ESO (representing its member states), NSF (USA), and NINS (Japan), together with NRC (Canada), MOST and ASIAA (Taiwan), and KASI (Republic of Korea), in cooperation with the Republic of Chile. The Joint ALMA Observatory is operated by ESO, AUI/NRAO, and NAOJ. CJU acknowledges support from TETFund, under the 2018 NEEDS intervention programme of the University of Nigeria, Nsukka.

DATA AVAILABILITY

The data used in producing the results in this article can be accessed from the Atacama Large Millimeter/submillimeter Array (ALMA). The raw data sets can be downloaded from the ALMA Science Archive whereas the calibrated and imaged data can be downloaded from this link: http://jvo.nao.ac.jp/portal/alma/archive.do.

REFERENCES

Arce H. G., Shepherd D., Gueth F., Lee C. F., Bachiller R., Rosen A., Beuther H., 2007, in Reipurth B., Jewitt D., Keil K.eds, Protostars and Planets V, University of Arizona Press, Tucson, p. 245

Bachiller R., 1996, ARA&A, 34, 111

Bachiller R., 2009, Astrophysics and Space Science Proceedings, Vol. 13. Springer, Berlin, p. 381

Bally J., Lada C. J., 1983, ApJ, 265, 824

Bøgelund E. G., Barr A. G., Taquet V., Ligterink N. F. W., Persson M. V., Hogerheijde M. R., van Dishoeck E. F., 2019, A&A, 628, A2

Brogan C. L., Hunter T. R., Cyganowski C. J., Indebetouw R., Beuther H., Menten K. M., Thorwirth S., 2009, ApJ, 707, 1

Burns R. A., Handa T., Nagayama T., Sunada K., Omodaka T., 2016, MNRAS, 460, 283

Caswell J. L. et al., 2010, MNRAS, 404, 1029

Cesaroni R., Galli D., Lodato G., Walmsley C. M., Zhang Q., 2007, in Reipurth B., Jewitt D., Keil K.eds, Protostars and Planets V, University of Arizona Press, Tucson, p. 197

Chen X., Gan C.-G., Ellingsen S. P., He J.-H., Shen Z.-Q., Titmarsh A., 2013, ApJS, 206, 22

Chibueze J. O. et al., 2017, ApJ, 836, 59

Chibueze J. O., Imai H., Tafoya D., Omodaka T., Kameya O., Hirota T., Chong S.-N., Torrelles J. M., 2012, ApJ, 748, 146

Csengeri T. et al., 2017, A&A, 600, L10

Csengeri T. et al., 2018, A&A, 617, A89

Csengeri T., Belloche A., Bontemps S., Wyrowski F., Menten K. M., Bouscasse L., 2019, A&A, 632, A57

Cunningham N., Lumsden S. L., Cyganowski C. J., Maud L. T., Purcell C., 2016, MNRAS, 458, 1742

Cyganowski C. J., Brogan C. L., Hunter T. R., Churchwell E., Zhang Q., 2011, ApJ, 729, 124

Cyganowski C. J., Brogan C. L., Hunter T. R., Zhang Q., Friesen R. K., Indebetouw R., Chandler C. J., 2012, ApJ, 760, L20

Di Francesco J., Evans N. J. I., Caselli P., Myers P. C., Shirley Y., Aikawa Y., Tafalla M., 2007, in Reipurth B., Jewitt D., Keil K.eds, Protostars and Planets V, University of Arizona Press, Tucson. University of Arizona Press, Tucson, p. 17

Gibb A. G., Hoare M. G., Little L. T., Wright M. C. H., 2003, MNRAS, 339, 1011

Ginsburg A., Bally J., Goddi C., Plambeck R., Wright M., 2018, ApJ, 860, 119

Herbst E., van Dishoeck E. F., 2009, ARA&A, 47, 427

Hildebrand R. H., 1983, QJRAS, 24, 267

Hunter T. R., Brogan C. L., Cyganowski C. J., Young K. H., 2014, ApJ, 788, 187

Ilee J. D., Cyganowski C. J., Nazari P., Hunter T. R., Brogan C. L., Forgan D. H., Zhang Q., 2016, MNRAS, 462, 4386

Johnston K. G. et al., 2015, ApJ, 813, L19

Johnston K. G., Hoare M. G., Beuther H., Linz H., Boley P., Kuiper R., Kee N. D., Robitaille T. P., 2020, ApJ, 896, 35

Khan S. et al., 2022, A&A, 664, A140

Kölligan A., Kuiper R., 2018, A&A, 620, A182

Liu T. et al., 2017, ApJ, 849, 25

Lucas P. W. et al., 2008, MNRAS, 391, 136

Martín-Hernández N. L., Vermeij R., van der Hulst J. M., 2005, A&A, 433, 205

Maswanganye J. P., Gaylard M. J., Goedhart S., Walt D. J. v. d., Booth R. S., 2015, MNRAS, 446, 2730

Mookerjea B., Casper E., Mundy L. G., Looney L. W., 2007, ApJ, 659, 447

Müller H. S. P., Schlöder F., Stutzki J., Winnewisser G., 2005, JMS, 742, 215

Osorio M., Lizano S., D'Alessio P., 1999, ApJ, 525, 808

Ossenkopf V., Henning T., 1994, A&A, 291, 943

Pickett H. M., Poynter R. L., Cohen E. A., Delitsky M. L., Pearson J. C., Müller H. S. P., 1998, JQS&RT, 60, 883

Rabli D., Flower D. R., 2010, MNRAS, 406, 95

Reid M. J. et al., 2014, ApJ, 783, 130

Reid M. J., Menten K. M., Brunthaler A., Zheng X. W., Moscadelli L., Xu Y., 2009, ApJ, 693, 397

Rong J. et al., 2016, MNRAS, 455, 1428

Sanna A. et al., 2019, A&A, 623, A77

Sugiyama K. et al., 2012, in Charlot P., Bourda G., Collioud A., eds, Proceedings of the 11th European VLBI Network Symposium and Users Meeting, SISSA Medialab srl Partita, Bordeaux-France, p. 32

Titmarsh A. M., Ellingsen S. P., Breen S. L., Caswell J. L., Voronkov M. A., 2016, MNRAS, 459, 157

Torrelles J. M. et al., 2011, MNRAS, 410, 627

Van der Tak F. F. S., Black J. H., Schöier F. L., Jansen D. J., van Dishoeck E. F., 2007, A&A, 468, 627

Van Der Walt S. J., Kristensen L. E., Jørgensen J. K., Calcutt H., Manigand S., el Akel M., Garrod R. T., Qiu K., 2021, A&A, 655, A86

Van Dishoeck E. F., Blake G. A., 1998, ARA&A, 36, 317
Walsh A. J. et al., 2011, MNRAS, 416, 1764
Walsh A. J., Purcell C. R., Longmore S. N., Breen S. L., Green J. A., Harvey-Smith L., Jordan C. H., Macpherson C., 2014, MNRAS, 442, 2240
Yang W., Xu Y., Chen X., Ellingsen S. P., Lu D., Ju B., Li Y., 2017, ApJS, 231, 20
Zhao B. et al., 2020, Space Sci. Rev., 216, 43
Zinnecker H., Yorke H. W., 2007, ARA&A, 45, 481

This paper has been typeset from a TEX/LATEX file prepared by the author.